Multichannel detection high-resolution electron energy loss spectrometer

Eue-Jin Jeong and J. L. Erskine

Department of Physics, University of Texas, Austin, Texas 78712

(Received 12 January 1989; accepted for publication 19 June 1989)

A new general-purpose high-resolution electron energy loss spectrometer has been constructed and tested. Novel features of the electron optics include multichannel energy detection and tandem four-element zoom lenses that incorporate beam defining apertures. Compact design of the lenses permit scattering measurements in which the total scattering angle is less than 40°. This feature permits probing bulk phonon modes. The lens system permits electronic adjustment of the analyzer collection angle, and yields high transmission at retardation/acceleration ratios of 400:1. Performance characteristics include simultaneous detection of 50 energy channels at 4-meV energy resolution and target currents exceeding 2×10^{-10} A. Separate monochromator and analyzer goniometers permit access to out-of-plane scattering configurations which enables probing odd symmetry shear surface modes.

INTRODUCTION

High-resolution electron energy loss spectroscopy (EELS) is now established as one of the most useful techniques for studying the physical and chemical properties of surfaces.[1,2] Recent reviews[3,4] and conference proceedings[5–7] document the new applications of EELS that continue to emerge as more versatile spectrometers which offer higher sensitivity and resolution have been developed. Advances in theoretical/numerical techniques for computing inelastic electron scattering cross sections,[8] surface vibrational properties,[9] and for analyzing EELS data[10] have accompanied improvements in instrumentation, and have helped stimulate the rapidly growing interest in the technique.

In spite of the significant advances in EELS spectrometer performance that have occurred since the technique was first introduced in the late 1960's, important new applications await additional improvements and many current applications could benefit from up-graded instrument performance and versatility. For example, intrinsic surface phonons and adsorbate phonon bands have been studied by several groups using EELS.[4,10–12] These experiments continue to be relatively tedious because of the low counting rates ($\sim10^2$ counts/s) that are achieved even by the best EELS instruments. Most surface phonon measurements carried out using EELS have been conducted at approximately 10-meV energy resolution rather than the ultimate resolution[13] ($\sim$2 meV) that has been demonstrated in EELS measurements. High resolution is traded off for intensity in order to achieve adequate counting rates. Inelastic He scattering measurements of surface phonons[14,15] carried out at submillivolt energy resolution have established the importance of high-energy resolution in this application. A good theoretical basis[16,17] exists for exploiting the angular dependence of elastic and inelastic electron scattering cross sections as a probe of molecular orientation on surfaces. However, lack of instrument versatility has limited this important application. Useful information related to the potentials that bind crystals and account for surface chemical bonds can be obtained from detailed analysis of surface vibrations and their overtones. Overtone loss features[18,19] are typically very weak (few counts/s) and closely clustered in energy. Extensive experimental studies of overtone losses clearly require improved EELS instrumentation. Surface vibrational studies of technical surfaces represent a potentially important new area in which the EELS technique could be exploited. Inelastic electron scattering counting rates from technical surfaces are low because diffuse scattering resulting from the surface roughness introduces a large angular spread in electrons scattered by the dipole scattering mechanism.[1–3,20]

Most EELS instruments have been designed for analyzing dipole scattering losses. The dipole scattering mechanism produces energy losses in a narrow beam centered along the specular direction.[20] In practical analyzers, the beam is narrow enough that essentially all electrons that experience dipole scattering losses are collected by the analyzer entrance slit.[3] Impact scattering losses[2–4,21] are characterized by large scattering angles. Accurate and effective measurements of impact scattering losses require different analyzer collection lens considerations than for dipole scattering measurements. Specifically, certain types of measurements require large collection angles to maximize sensitivity (technical surfaces), and some require very narrow or well-defined collection angles (mapping surface phonons and studies of angle and energy dependent inelastic scattering cross sections). In general, inelastic scattering losses measured in the impact scattering regime require operating the EELS optics at relatively high impact energies (several hundred electron volts) where impact scattering cross sections are large. The high deceleration ratios needed to maintain adequate energy resolution must also be considered in the lens system design.

From the few examples just presented, and the enormous success that inelastic electron scattering techniques has achived in the study of surface properties, it should be clear that efforts to improve performance levels of EELS instruments are justified. The purpose of this article is to describe a new inelastic electron scattering spectrometer that is more versatile and achieves better performance than other existing instruments. The new spectrometer is a general purpose instrument designed primarily to study surface phonon dispersion and inelastic differential scattering cross

 0034-6748/89/103139-12$01.30

sections. In its present configuration, it is not optimized for applications generally dependent on measuring strong dipole scattering losses because of the upper counting rate limit that can be achieved by the position sensitive detector.

I. EVOLUTION OF EELS INSTRUMENTS

Many important improvements in EELS instruments have been introduced since the first observation of surface vibrational modes by Propst and Piper.[22] Froitzheim *et al.*[23] developed one of the first high performance EELS instruments that permitted routine analysis of surface vibrations in the dipole scattering regime. Many of the instruments that have been developed since 1975 when this instrument was introduced still bear striking resemblance to their original design. Characteristic features include the electron gun design, 127° energy dispersing sectors, and plate lenses. In 1983, Lehwald *et al.*[24] reported the first observation of surface phonons using EELS, which required extending the impact energy range to several hundred eV.

A significant departure from the conventional Froitzheim-Ibach instrument was introduced by Ho's group in order to improve the overall instrument sensitivity and permit time-resolved experiments.[25,26] The principle new feature involved adapting multichannel energy detection to a large hemispherical analyzer. A similar instrument incorporating multichannel detection in a 127° sector was reported by Franchy and Ibach.[27] The concept of using position sensitive detection techniques in charged particle and photon detection to increase sensitivity of spectroscopic techniques dates back to the introduction of imaging quality microchannel plates.[28] Richter and Ho[29] and Asplund *et al.*[30] have written up-to-date reviews dealing with implementation of position sensitive detection in EELS and x-ray photoelectron spectrometers, respectively. A completely different method for improving the sensitivity of EELS instruments based on the principle of dispersion compensation has been explored by Kevan and Dubois.[31] Although this design probably offers the best prospects for high sensitivity (required for time-resolved measurements), it is not particularly well suited for achieving the high enregy and angular resolution required for surface phonon measurements and cross-section measurements.

The instrument described in the present article has been developed to fill a specific need in the field of EELS applications. Our primary objective was to set up an instrument optimized for studying surface and interface phonons, and for measuring impact scattering differential cross sections. Several factors account for the improved performance that our new instrument achieves. Sensitivity is improved by combining a high-current monochromator with a multichannel detection energy analyzer. High-energy resolution is obtained by using large mean radius hemispherical capacitors and by careful attention to field terminations at slits and at the position sensitive detector. Improved instrument versatility and performance is obtained by introducing compact high-performance tandem zoom lenses in the monochromator and analyzer optics. These lens systems yield acceleration/deceleration ratios of several hundred to one while maintaining good imaging characteristics and high transmission. A versatile combination of goniometers permits out-of-plane scattering geometry to be conveniently achieved, permitting measurements of shear modes and related experiments in which scattering selection rules can be exploited.

II. DESCRIPTION OF SPECTROMETER

Our EELS spectrometer is mounted in an 18-in.-diam mu-metal vacuum chamber purchased from Vacuum Generators, UK. We found that satisfying the magnetic shielding requirements by employing a vacuum chamber fabricated from mu-metal was cost effective for a large chamber. Magnetic fields inside the chamber have been measured using a Hall probe (Bell Model #640) and found to be well below 10 mG. As discussed later, we have achieved energy resolution of below 4 meV at 1-eV pass energies. The measured current from the monochromator as a function of pass energy does not depart from expected behavior for pass energies as low as 0.2 eV. Therefore, it is clear that the magnetic shielding is more than adequate for any intended EELS applications. No external coils or seperate ion pump magnetic shields are employed.

Figure 1 displays the principle features of the vacuum chamber. The mu-metal chamber is pumped by a 1200 l/s ion pump that has an internal liquid N_2-cooled titanium sublimation pump. The preparation chamber is pumped by a 400 l/s ion pump and a turbomolecular pump. A gate valve separates the EELS chamber from a preparation chamber that provides standard sample preparation and characterization capabilities including molecular beam epitaxy, low-energy electron diffraction, Auger electron spectroscopy, ion sputtering, and mass spectroscopy. The probe arm allows electron beam heating, cooling to 80 °K and a single rotational degree of freedom around the translation (z) axis.

The EELS optics are mounted on manipulators designed to facilitate alignment and to provide access to a variety of scattering configurations. Figure 1 also indicates the various degrees of freedom associated with the sample manipulator, the monochromator, and the analyzer. The monochromator rotation table located inside the mu-metal chamber is mounted on an external linear translation device that permits $\pm$ 1/4 inch of motion in the xz plane. Two translational degrees of freedom are necessary because the monochromator and analyzer are mounted on separate flanges (one is a large wire seal flange), and the acceleration and deceleration lens systems define highly directional incident and detected beam axes. Sight holes in the monochromator and analyzer electrostatic shields (1/4 in. diam) and outer hemispheres (No. 80 drill size) permit accurate mechanical alignment in direct beam geometry. The analyzer is mounted on a rotation stage having an axis (x axis) perpendicular to the monochromator rotation axis (z axis). This arrangement permits out-of-plane scattering to be studied.

The electron analyzer and monochromator consist of identical hemispherical capacitors and identical tandem four-element zoom lenses. Figure 2 presents a schematic drawing of the principle features of the electron optics which are shown in direct beam geometry. The electron gun and premonochromator are essentially identical to the original

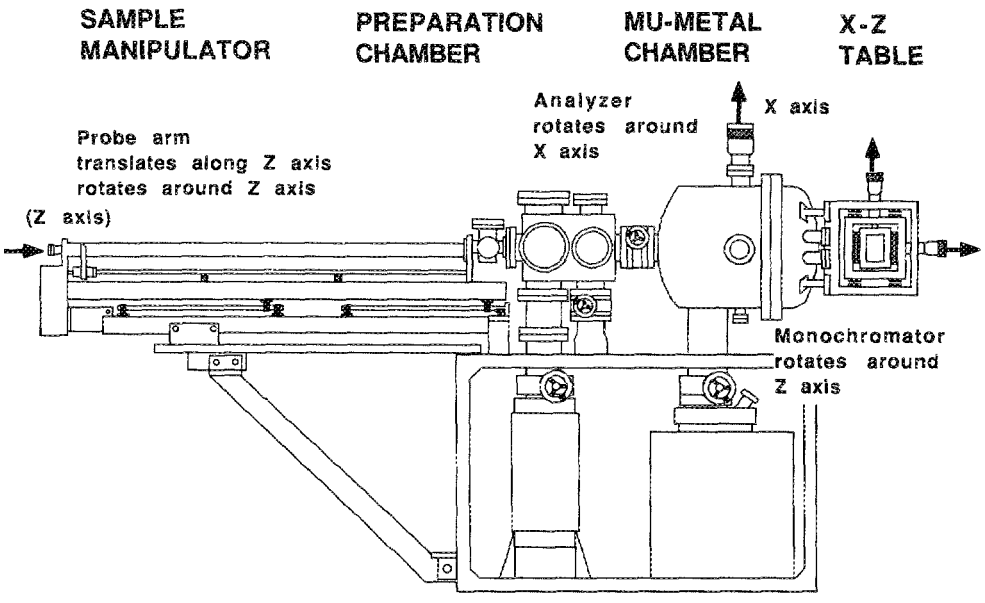

FIG. 1. Schematic diagram showing principle features of EELS spectrometer vacuum chamber and the rotational degrees of freedom of monochromator, analyzer, and sample manipulator.

single 127° cylindrical sector design developed by Froitzheim *et al.*[23] The premonochromator is coupled to the main (hemispherical capacitor) monochromator by a three-element lens system. Identical tandem four-element zoom lenses separated by apertures are used to accelerate electrons from the monochromator exit slit to the target, and to decelerate scattered electrons from the target to the analyzer entrance slit. Both monochromator and analyzer are enclosed in electrostatic shields. Table I summarizes the principal geometrical parameters of the electron optics and specifies the range of scattering parameters accessible by our instrument. The following sections present details covering the zoom lens system, the premonochromator, and the multichannel detection system including field termination at the channel plates.

III. PREMONOCHROMATOR

Previous practical experience[32,33] and analysis[34,35] have established the benefits of using a premonochromator to supply electrons to the entrance slit of an electron monochromator. Mutual repulsion of electrons in a high current density electron beam (space charge effects) limits the amount of current that can be passed through a fixed volume

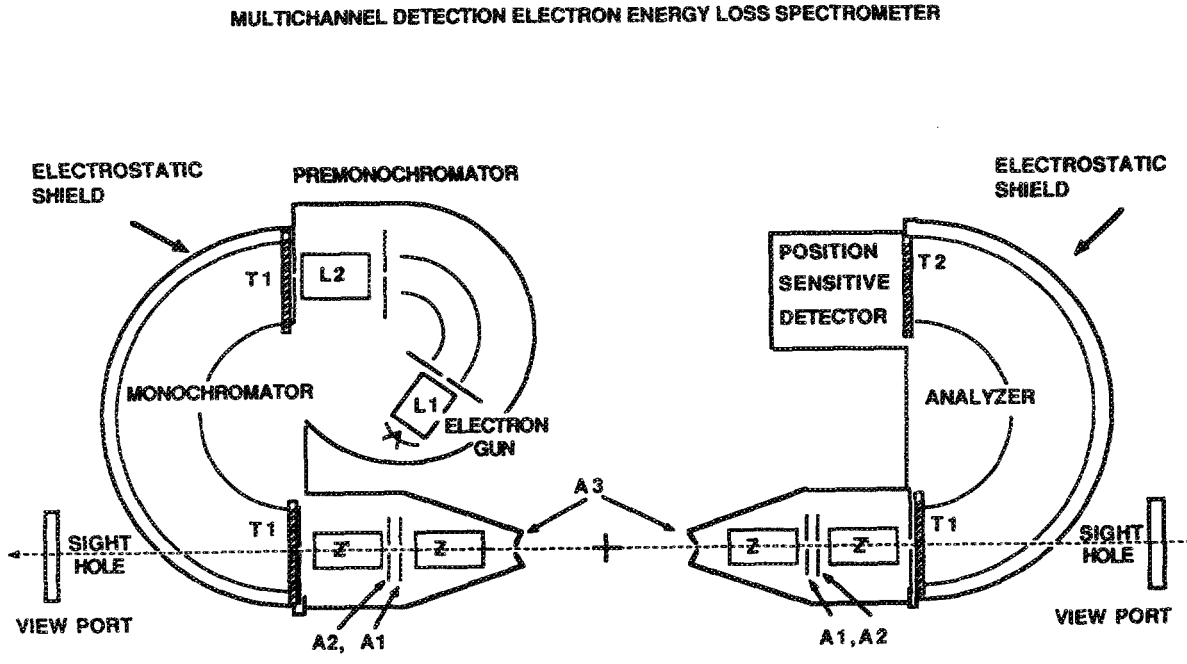

FIG. 2. Schematic diagram of multichannel detection electron optics. Refer to text for details. L_1 five-element lens, L_2 three-element lens, Z, Z', four-element zoom lens, A_1, A_2, A_3, beam defining apertures; T_1, T_2, field terminators.

TABLE I. Electron optics parameters. Scattering geometry restrictions: In plane scattering limitations: $\theta_{inc} + \theta_{Scat} \geqslant 30°$, out of plane scattering with $\theta_{inc} = 0$ normal beam incidence: $\theta_{Scat} > 30°$.

Premonochromator	R_1	1.240 in.
	R_2	1.634 in.
	R_0	1.437 in.
	w(slits)	0.027 in.
	h(slits)[b]	0.200 in.
Main monochromator and main analyzer	R_1	2.25 in.
	R_2	3.25 in.
	R_0	2.75 in.
	w(slits)[a]	0.015 in.
	h(slits)	0.150 in.
Resistive field termination	Material:	0.02-in. thick Mica or Teflon sheet uniformly coated with graphite
	Aperture:	1×0.2 in. rectangle
	Resistance:	100–500 Ω between inner and outer hemispheres
Position sensitive detector	Surface Science Laboratories (Ref. 41) Model No. 3390 OPT SA (1 in. diam) Spatial Resolution: 200 line pairs/in. Field Termination: refer to text	

[a] Curved with radius $R_0/2$ (refer to Ref. 42).
[b] Rectangular.

at a given beam kinetic energy. When the volume is defined by two apertures of diameter d separated by a distance l, the maximum monochromatic current which can be transmitted is given by[36]

$$I_{max} = 38.5E^{3/2}(d^2/l^2) = 38.5E^{3/2}\alpha^2 \quad (1)$$

where units of I_{max} and E are microamps (μA) and electron volts (eV), respectively. The alternate form of Eq. (1) is obtained by replacing (d^2/l^2) by α^2 where α is the beam angle. An analysis of monochromator performance by Froitzheim[34] that includes space charge considerations has suggested that optimum performance from a charged particle monochromator is obtained when the monochromator (entrance slit) is operated just below the space charge saturation condition. The purpose of the premonochromator and coupling lens system is therefore to: 1) provide a beam of electrons at the monochromator entrance slit that has the maximum angular width allowed by the resolution limiting acceptance conditions of the monochromator, and 2) focus at the slit only those electrons having kinetic energy in a narrow band around the pass energy of the monochromator. These conditions minimize broadening of the monochromatic beam by space charge effects.

Our electron gun is similar to the one described by Froitzheim.[37] It consists of a tungsten hairpin filament, a repeller, and a five element lens which provides focusing and deflection steering parallel and perpendicular to the premonochromator entrance slit axis. The premonochromator is based on a 127° cylindrical capacitor design described by Froitzheim *et al.*,[23] including a fine sawtooth corrugation milled in the sector walls to reduce electron reflections through the exit slit. Fringing field corrections in the premonochromator were implemented according to work reported by Wollnick and Ewald[38] and by Herzog.[39]

A three-element intermediate lens between the premonochromator exit slit and main monochromator entrance slit permits operating the two monochromators at different pass energies.[34,35] This lens provides efficient coupling of the premonochromatized beam into the main monochromator. Out-of-plane focusing by the intermediate lenses (as described by Kesmodel[33]) is unnecessary in the present design because the main (hemispherical) monochromator offers stigmatic focusing between entrance and exit slits. The electron gun provides sufficient out-of-plane focusing at the premonochromator entrance slit that the most intense part of the beam at the monochromator entrance slit can be made less than the slit height.

Figure 3 displays the current from our monochromator measured by a Faraday cup collector placed at the target point as a function of monochromator resolution. The Faraday cup intercepts all electrons from the monochromator as well as secondary electrons produced within the cup by the monochromatic beam. The net current to ground is equal to the true monochromator current minus the negligible secondary electron current that escapes through the Faraday cup aperture. The slope of the current versus resolution curve obtained from the log-log plot of Fig. 3 is 1.7, suggesting a slight departure from the expected $J\alpha E^{3/2}$ behavior.

Analysis of monochromator behavior by both Froitzheim[34] and by Unwin *et al.*[35] suggests that (under suitable conditions) the gain in the usable current that can be realized by adding a premonochromator is

$$\text{Gain} = (E_0/E_1) \quad (2)$$

where E_0 and E_1 are the premonochromator and main monochromator pass energies. Figure 4 displays premonochromator and monochromator currents as a function of premonochromator pass energy. The monochromator pass energy was held constant at 1 eV for these tests. Premono-

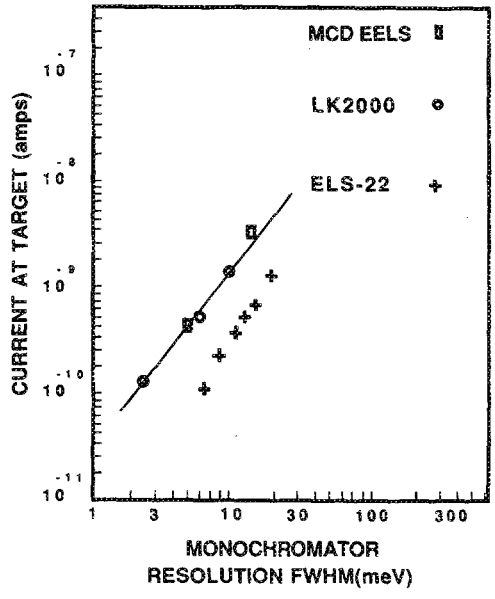

FIG. 3. Target current vs resolution of monochromator for three EELS instruments. ELS-22 (Leybold-Heraeus instrument), LK 2000 (tandem monochrometer instrument described by Kesmodel, (Ref. 33), MCD EELS (instrument described in present article).

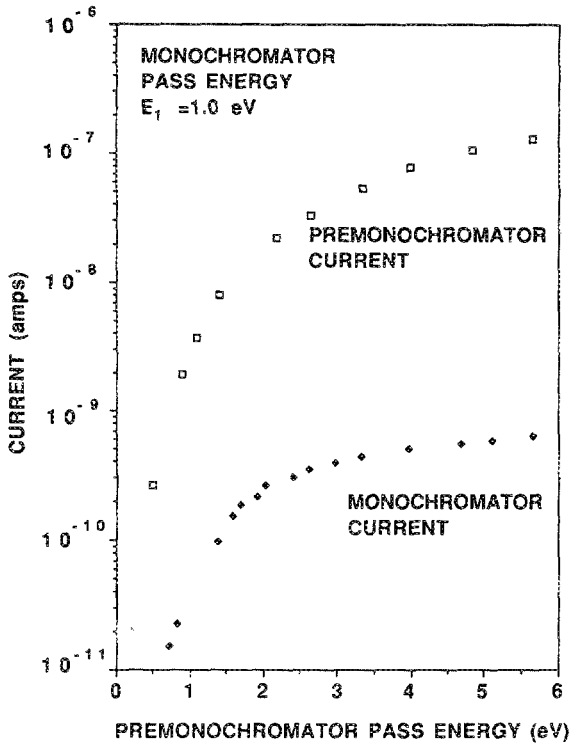

FIG. 4. Plot of current from premonochromator and from main monochromator vs premonochromator pass energy. Monochromator pass energy is held fixed at $E_1 = 1.0$ eV for monochromator current tests.

chromator output current was measured at the outer hemisphere of the monochromator; monochromator current was measured at the target position. These curves characterize our monochromator performance. A monochromator pass energy of $E_1 = 1.0$ eV yields a (theoretical) energy resolution of $\Delta E \sim 2.7$–5.0 meV depending on the contribution from the angular spread of the electron beam entering the slit. Polaschegg[40] has shown (neglecting space charge effects) that maximum luminosity (product of flux and energy resolution) occurs when $w/2r_0 = \alpha_{\max}^2$ where the parameters w and r_0 are defined in Table I, and α is the beam angle at the slit. We have found, after tuning the instrument repeatedly and after several months of practical operating experience, that for $E_1 = 1.0$ eV, the best performance (intensity and resolution) occurs for premonochromator pass energies of $E_0 \sim 2$–3 eV. Based on Eq. (2), this corresponds to an improvement of a factor of two to three in performance over a single monochromator based spectrometer.

It is clear that the results of Fig. 4 (as well as the corresponding results presented by Froitzheim[34]) do not support the simple E_0/E_1 gain in performance. Froitzheim's analysis suggests the current should be proportional to $E_0 E_1^{3/2}$ (linear in E_0 for fixed E_1). Our results suggest optimal results near the knee of the curve away from the linear regime. This result suggests a more thorough analysis may be required to understand optimal conditions for operating a two-stage monochromator.

It is interesting to note that there are several differences between the three instruments for which monochromator performance is displayed in Fig. 3. One difference is the mean radius of the main monochromator. The LK 2000 and our MCD instruments have comparable mean radii, whereas the ELS-22 has a main monochromator mean radius approximately equal to that of our premonochromator (roughly a factor of two smaller). In addition, in our ELS-22, the premonochromator and main monochromator share a common slit and must be operated at the same pass energy. The difference in performance between the ELS-22 and the other two monochromators can be understood as a consequence of larger monochromator radius (factor of two) and the capability to operate a premonochromator at a different pass energy than the main monochromator (factor 2–3). Both of these differences result in a larger phase space of the source flux being effectively coupled into the monochromator entrance slit under space charge limited conditions. Apparently out-of-plane focusing by the intermediate lens system of the LK 2000 compensates for the absence of stigmatic focusing in the main monochromator that our hemispherical design offers.

IV. ANALYZER AND MAIN MONOCHROMATOR

The main monochromator and the energy analyzer are based on 180° hemispherical capacitors. A standard commercially available position sensitive detector[41] is used for multichannel detection. Analysis of the image properties of a hemispherical capacitor[42,43] has established the feasibility of high-resolution multichannel detection in an EELS instrument as well as the criteria for achieving optimum performance. Aberrations in the entrance slit image across the exit plane of the hemispherical analyzer are small enough that most of the area can be used for detection. Also, the energy dispersion at the exit plane is nearly linear, as will be discussed later. The angular spread of electron trajectories can cause problems at the position sensitive detector edges that result from reflections at the hemispheres if the gap is not sufficiently larger than the detector width. Fringe field effects at the slits and detector plane are key issues that are discussed in a following section. There are two approaches to the fringe field problem in single channel (all slit) spectrometers. One approach is based on the work of Herzog[39] and others who have shown that the effects of fringe fields can be compensated by introducing a suitable gap (Herzog correction) between the capacitor and the slit plate, or by a slight change in the sector angle. A second approach is to design a suitable field termination at the slits and detector.[26,42,44] This approach, though less elegant is more universal (i.e., does not depend on mean radius to gap ratio), and can be applied at both the slits and the position detector. In addition, in instruments designed for multichannel detection, the gap-to-mean-radius ratio is large[42] for optimum performance. Field penetration problems are therefore more severe than in the case of single channel instruments which require only that the gap is large enough to accommodate the desired angular acceptance.

Mechanical construction was greatly simplified by electing to use full 180° hemispheres. The capacitors and hemispherical electrostatic shields are "as delivered" 0.010-

in.-thick hydroformed copper hemispheres obtained from Krupp & Sons. Precision measurements determined that the shape was spherical to approximately ± 0.001 in. The most serious departure from a hemispherical shape was a small elliptical distortion in the plane perpendicular to the rotational symmetry axis. This distortion was easily corrected by the method used in mounting the hemispheres. Each hemisphere was mounted to a plate via insulated screws. The hemispheres were indexed to the plate via eight 1-mm diam sapphire balls that resided in precisely indexed cone shaped holes (refer to Fig. 5). When the holes were milled in the lip of each hemisphere, the hemisphere was clamped in a device that forced the lip to assume a precise circular shape. When mounted to the plate, the sapphire balls forced the hemispheres to assume the desired perfect circular shape.

Most of the electron optics are fabricated from copper; tantalum and molybdenum parts are used in the electron gun and slits. Standard stainless-steel screws are used throughout the electron optics. The stainless-steel screws exhibited weak magnetic behavior; therefore, the size of each screw was maintained at the minimum required for each application. Sapphire balls, macor machinable glass and mica are used as insulating materials. All wires that provide bias voltages are electrostatically shielded from regions where electric fields are required to guide electron trajectories. All electron optical elements are surrounded by grounded enclosures that maintain a field free region inside the mu-metal chamber.

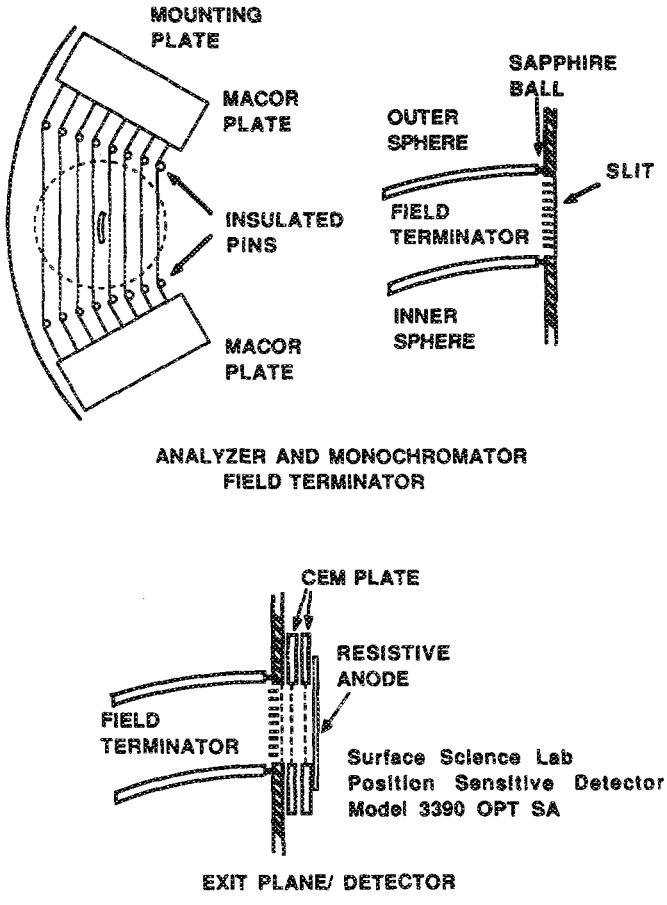

FIG. 5. Construction details describing field terminators at monochromator and analyzer slits, and at the position sensitive detector. Slit field terminators consist of 8 1×10-mil^2 W ribbons stretched between insulating pins. The position sensitive detector terminator is the same geometry but includes a second terminator consisting of a high transmission grid (90%) between the ribbons and the first channel plate. Total distance from ribbons to channel plate is about 2 mm.

V. FIELD TERMINATIONS

Electrostatic deflection analyzers and monochromators require an effective means of dealing with the fringe field problem. These effects have also been treated in some detail in relation to multichannel energy detection in previously reported work.[25,26,42,44,45] The origin of fringe fields and the adverse effects the fields have on electron trajectories are easy to visualize by referring to the hemispherical analyzer in Fig. 2. The entrance slit and the channel plate detector can be regarded as equipotential planes that strongly perturb the r^{-1} potential produced by the electrically biased hemispheres. These field perturbations alter the trajectories and affect the focusing properties of the analyzer.

The influence of slit fringing fields on charged particle trajectories has been studied repeatedly. The most generally accepted method for dealing with fringing field effects is based on the work of Herzog.[39] Effects of fringe fields are minimized by implementing a slit geometry that is effective in maintaining the correct potential along the mean radius which intersects the slits. Recent studies based on numerical calculations of electron trajectories through cylindrical capacitor analyzers[46] and hemispherical analyzers[43] have been successful in optimizing the Herzog correction and sector angles for slit plate fringe fields. In cylindrical capacitor analyzers, an optimum focus occurs at a deflection angle of 127.3° when no fringing fields are present. Oshima *et al.*[46] have shown that for practical ratios of gap-to-mean radius (assuming single channel detection instruments), a deflection angle of 126.5° combined with a Herzog correction yields the same degree of beam focusing as in the ideal field case. A corresponding analysis by Nishigaki and Kanai[43] for a 180° deflection hemispherical analyzer has yielded optimization criteria for the Herzog region and the electrode sector angle. With suitable Herzog regions that depend on the gap-to-mean radius ratio, a practical hemispherical analyzer yields focusing equal to the ideal field case for a sector angle of 174.2°.

Field termination at a position sensitive detector presents a more difficult problem which has not been treated in the same detail as the slit termination problem. Adequate termination at a position sensitive detector is particularly difficult in an EELS analyzer. Efficient electron detection by channel plates requires incident kinetic energies of about 50 eV. An electrostatic deflection analyzer operating at low-pass energies (~ 1 eV) requires a 50-eV accelerating potential between the hemispheres and the first channel plate. In addition, the transformation from a r^{-1} potential perpendicular to the electron orbit to a strong electric field parallel to the trajectory must occur over a distance short enough that the image properties of the analyzer are not affected. The energy resolution and linear dispersion of electron energies along the exit plane of the capacitor must be preserved for

good energy resolution and simplified image processing.[42]

Our approach to the field termination problem is based on maintaining 180° deflection analyzer geometry and setting up appropriate electrodes to preserve the r^{-1} potential at the entrance slit of the analyzer and at the position sensitive detector. The main monochromator is identical to the analyzer, and both monochromator slits are terminated in a manner identical to the analyzer entrance slit: All three spherical analyzer slits are terminated by an array of eight equidistant 1×20 mil tungsten ribbons parallel to the slits that are electrically biased by a resistor network outside of the vacuum chamber to best approximate a r^{-1} potential in the plane of electron orbits.[42] In each case, the slit lies between the central pair of ribbons. Figure 5 illustrates the configuration of field terminations used in both the monochromator and analyzer.

Several analyzer exit plane field terminators were evaluated. One configuration consisted of the same 8-ribbon array used at the slits followed by a fine wire mesh (90% transmission) electrically biased at the slit potential. The geometry of this configuration was basically the same as the one previously analyzed by ray tracing[42] which is detailed in Fig. 5. This configuration produced excellent images between the ribbons but suffered from broadening of the images by scattering near the ribbons. A second configuration in which the center section of each ribon was removed leaving a gap approximately equal to the height of the entrance slit was also evaluated. This configuration yielded good performance. The periodic distortion of the entrance slit image across the position sensitive detector was reduced below detectability. A third field termination was investigated in some detail and was used in obtaining experimental results displayed in Figs. 8–11. This termination consisted of a resistive plate clamped between the inner and outer spheres with a slot cut out to permit electrons to pass through the high-transmission grid to the channel plates (refer to Table I). This field terminator produces a $\ln(r)$ potential rather than the ideal r^{-1} potential. However, the r^{-1} and $\ln(r)$ potentials are very similar when constrained at the hemisphere potentials (refer to Fig. 6). This termination yielded excellent performance. Obvious refinements of the resistive termination that corrects the fields errors have not been implemented at present. Tests of the dispersion of energies across the detector plane discussed in a following section suggest that improvements are not necessary.

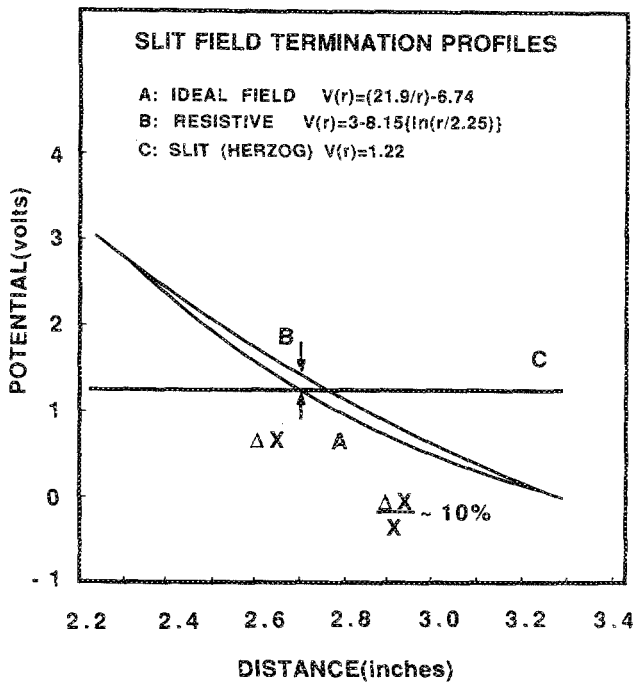

FIG. 6. Plot of potential vs distance (between hemispheres) measured from center of sphere for a r^{-1} (hemispherical capacitor) and a $\ln(r)$ resistive sheet clamped between hemispheres.

VI. ZOOM LENS SYSTEM

The monochromator and analyzer are equipped with an identical tandem four-element cylinder lens system detailed in Fig. 7. This lens design is similar to one described by Kevan[47] which is based on tandem three-element lenses. All lens elements and bias wires are enclosed in a grounded cone shaped shield. The lens system has provisions for placing one or two apertures between the tandem lenses without disassembly. The two lens elements nearest the slits are split perpendicular to the slit axis (nearest lens) and parallel to the slit axis (next nearest lens) to permit beam steering between the apertures and the slits. No provisions for beam steering are incorporated in the lenses between the apertures and target. This feature is intended to preserve angular accuracy of the instrument. A complete discussion of the lens system[48] and its properties are beyond the scope of the present article. Recent papers describe characteristics of four[49,50] and five[51] element tube lenses similar to the lenses used in our electron optics and more details about our lens system will be reported elsewhere.[52] Therefore, the following discussion only outlines the rationale for adopting the tandem four-element configuration, and describes some of the useful properties of the lens system.

The monochromator and analyzer lenses serve complementary functions. The monochromator lens system must form an image of the exit slit at the sample as well as accelerate electrons from the pass energy to the desired incident energy $E_{\rm inc}$. The beam area A_s on the sample defines the source brightness viewed by the analyzer; therefore, it is important that this area be as small as possible. The angular spread of electrons incident at the target is also important when performing experiments in which momentum transfer parallel to the surface is an important parameter, (i.e., mapping surface phonon dispersion).

The analyzer lens system must accept scattered electrons from the target area A_s in a defined solid angle Ω_s and focus them through the entrance slit. The electrons must also be decelerated to the analyzer pass energy. Depending on the particular experiment being conducted, it may be necessary to restrict Ω_s (in cases where momentum transfer is important) or to make Ω_s a maximum to optimize the collected electron flux. Clearly, there are a number of parameters that the lens systems must effectively deal with: acceleration/deceleration ratios, linear and angular magnification ratios, and source-to-image distances. In addition,

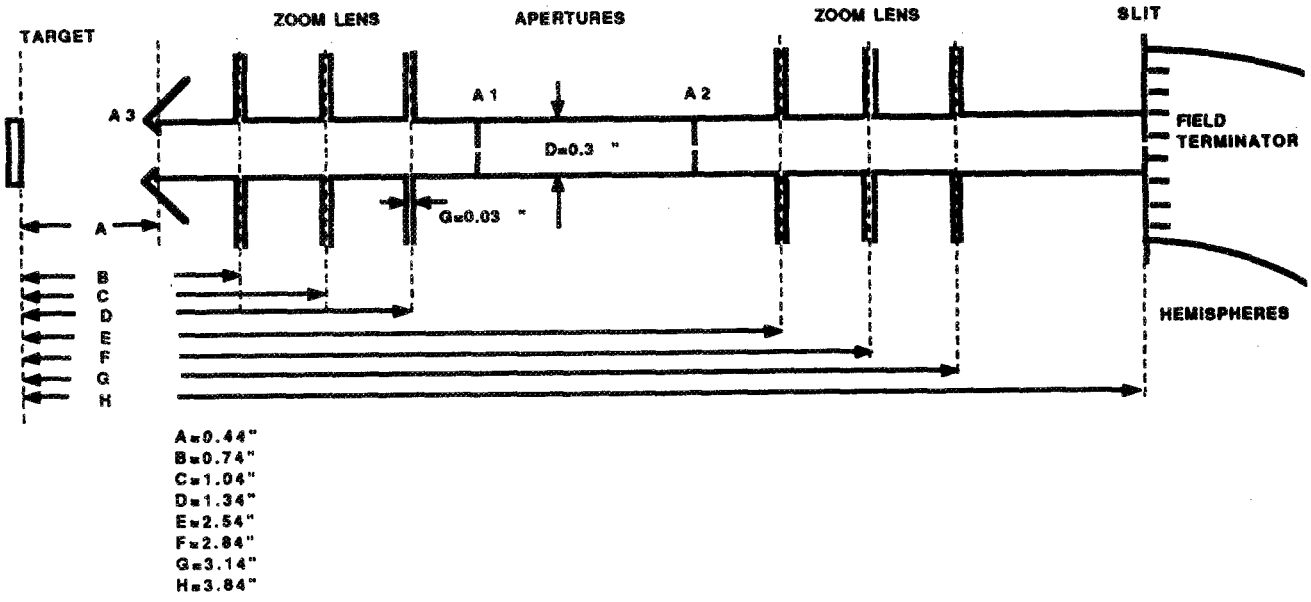

FIG. 7. Scale drawing of tandem four-element cylinder lens system used in monochromator and analyzer.

when a lens system is used in conjunction with multichannel detection, chromatic effects introduced by the lens system at the analyzer entrance slit become important. An ideal lens system would yield an image of the source at the entrance slit that maintained the same focal properties (shape, depth of field) over the window of energies being detected by the multichannel detector. In a single channel instrument, the corresponding energy window is small (and equal to the analyzer resolution). One of the reasons for using a more complex lens system (than is traditionally used in EELS instruments) is that lenses having more elements generally are capable of yielding better performance in all of the critical areas described above than simple two or three element lens systems.

A lens operated in a mode that maintains a fixed image position while varying the kinetic energy ratio is referred to as a zoom lens. Three element lenses offer two variable voltage ratios, and can be used to focus a beam of electrons in a manner that preserves the image position while varying the ratio of initial to final kinetic energy. In three element lenses, the linear and angular magnifications are not constant. For applications that require two parameters to remain constant (i.e., the image position and magnification) while varying the kinetic energy, a third variable voltage ratio is necessary, and the lens must consist of at least four elements. Additional lens elements also extend the deceleration range over which good image properties can be obtained for a fixed image distance. Recent experimental studies[51] have shown that a five-element lens can be operated to yield good transmission and constant magnification over a deceleration range of 1000–1.

Properties of the tandem four-element zoom lens illustrated in Fig. 7 have been investigated using ray tracing,[48] and by empirical tests.[52] Real apertures between the tandem lenses require lens modes that position an image at the aperture for high transmission. This constraint, plus the ability to view the image of the elastic peak at the analyzer exit plane, provide a convenient and effective means of optimizing a lens operating mode at a given incident energy. Poor focusing at the analyzer entrance slit or a beam angle that exceeds α_{max} will decrease intensity and cause broadening of the exit plane image. Under ideal conditions, a sharp rectangular image of the entrance slit can be achieved with a definition that is limited by the detector spatial resolution (200 line pairs per inch). Preliminary tests of the lens system have established that the transmission of each tandem lens is approximately 70% with a 0.05 in. diameter beam-defining aperture in place (A_2). The monochromator current, $I_{inc} = 9.2\times10^{-10}$ amp (at $E_0 = 0.97$ eV), was measured at A_2 by grounding that lens element through an electrometer after tuning the instrument in direct beam geometry. The corresponding current at the first channel plate was $I_{det} = 3.2\times10^{-10}$ amp corresponding to a total instrument transmission of $\sim 30\%$. (A small intensity loss occurs at the analyzer entrance slit due to image aberrations.) The acceleration/deceleration energy for these tests was ~ 170 eV, but similar results were obtained at other energies. There is no assurance that the lens tuning was optimized during these tests: no aperture was placed at the target position to require a focus at that location. However, the lens voltages were set to values that had previously yielded good intensity under actual scattering conditions, and these conditions correspond to symmetric voltage settings of the monochromator and analyzer lenses. The operating modes of the tandem lens system will be described in a separate publication.[52]

VII. ELECTRONICS/CONTROL

A computer is required to process data from the position sensitive detector. Our control electronics are based on an LSI-11/23 microcomputer interfaced to a CAMAC crate. Premium quality modular power supplies connected to rela-

tively low-resistance (several kΩ) potentiometers are used to provide voltages for the 127° sectors, hemispheres, monochromator coupling lenses, and electron guns. Provisions for eventually controlling the acceleration optics and energy defining slits by computer driven precision power supplies have been included in the design. At present, only the sweep voltage generated by an optically isolated operational amplifier is under computer control. Voltage ripple and noise on all wires that operate the spectrometer are below 0.5 mV. The computer software includes an energy calibration subroutine and a subroutine to overlay data from the multichannel detector in such a manner that gain variations over the channel plate area do not affect the spectra. In spite of the large number of voltages required to operate the optics, the beam can usually be found and optimized in a matter of minutes.

VIII. PERFORMANCE

Our new instrument has been in operation approximately six months (at this writing); therefore, the performance achieved to date and reported in this section may be regarded as conservative. We have not fully explored the range of options for operating the electron optics, and continue to learn more about factors that affect performance. However, our preliminary results clearly represent a significant improvement in EELS instrument performance.

In order to determine the inherent spectrometer characteristics, we conducted tests in "direct beam" geometry. These experiments primarily test the ultimate spectrometer resolution and lens transmission characteristics, and address issues pertaining to field terminations and properties of the multichannel detection. Space charge effects do not significantly affect the spectrometer performance in direct beam geometry experiments because the monochromator must be operated at very low currents (10^{-3} of optimum current) to avoid detector saturation. Thus, spectrometer characteristics measured in direct beam geometry provide a baseline performance level to seek in scattering experiments. Figure 8 displays a set of six direct beam spectra for various analyzer slit settings. The analyzer and monochromator pass energies were set at 1.2 eV. This pass energy corresponds to a theoretical analyzer resolution of 1.64 meV if the α^2 term is small in Eq. 2, or 3.27 meV if angular and slit width factors contribute equally.

In a single channel instrument, with both analyzer and monochromator operating at the same energy resolution, the overall resolution will be $\sqrt{2}$ times the resolution of each device. In Fig. 8, the typical resolution is approximately 4 meV. Optimization of the lens tuning in straight-through geometry apparently results in a smaller α^2 contribution to the energy resolution than expected under conditions of maximum performance ($\alpha^2_{\max} = w/2r_0$). The energy resolution of the monochromator and analyzer are each of the order of 4.0 meV/$\sqrt{2}$ = 2.8 meV. The "incident" energy is 30 eV representing an energy which is intermediate between 1–2-eV energies used for "dipole" scattering experiments, and 100–400 eV energies required in "impact" scattering experiments. The total energy range of the position sensitive detector face at 1.2-eV pass energy is 256 meV. It is clear that the energy resolution varies by approximately 20% over the detector face. At 4-meV resolution, a 256-meV total energy range yields 64 energy channels. A few energy channels near the detector edges are not used, even though there is no evidence of significant image distortion or spurious background problems.

Background wings are present on either side of the direct beam image. For a given peak with a full width at half maxi-

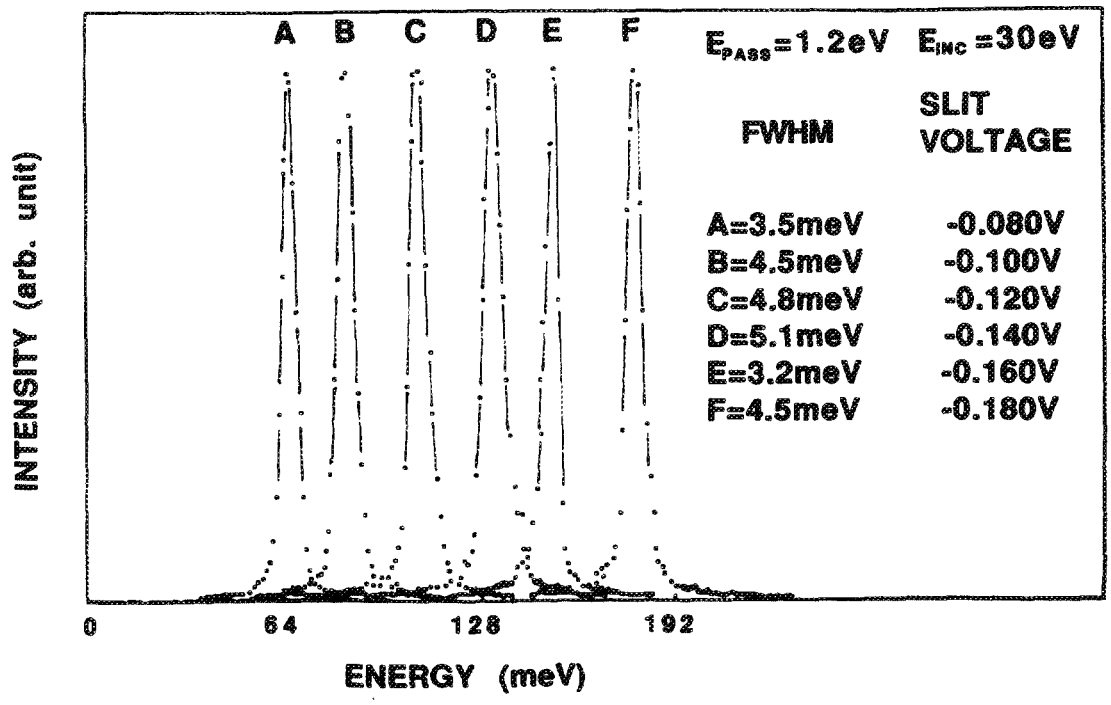

FIG. 8. Direct beam tests of analyzer resolution. Each peak corresponds to the elastic peak for a different analyzer slit setting.

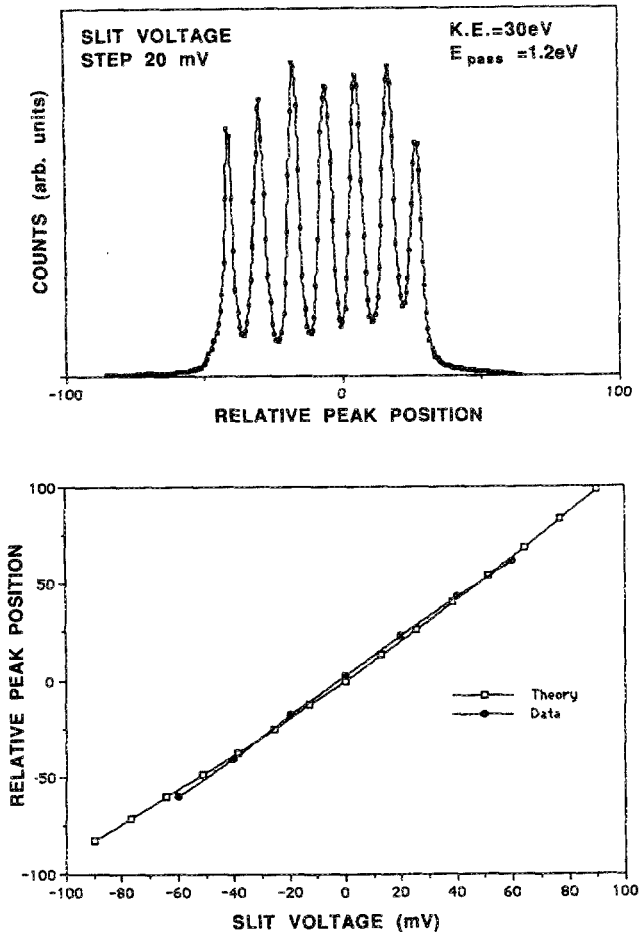

FIG. 9. Calculated (refer to text) and measured energy dispersion across the position sensitive detector. Upper figure displays elastic peak positions vs slit voltage; lower figure displays calculated image position and measured image position.

mum value of $\Delta E_{1/2}$, the wings are characterized approximately by the following: full width at 10% maximum, $(2\Delta E_{1/2})$; full width at 5% maximum $(3\Delta E_{1/2})$; and full width at 1% maximum, $(8\Delta E_{1/2})$. We do not know why the wings on our spectra are more pronounced than in single channel (all slit) instruments. We have noted significant improvements by adjusting the channel plate bias voltages and the acceleration voltage (between slit and channel plates) but prefer not to speculate on the origin of this effect until we understand it.

Figure 9 displays the predicted and measured energy dependence of the image location along the position sensitive detector. The measured values are taken from results shown in Fig. 9(a). Predictions are based on the following formula[42] that applies to trajectories of electrons in a hemispherical capacitor:

$$\xi_{\mathrm{EXIT}} = -\xi_{\mathrm{ENT}} - 2\{1 - 1/[1 + \sin^2\alpha - (\Delta E/E_0)(1 - \sin^2\alpha)]\}. \quad (3)$$

In this expression, α is the angle (in the plane of the orbit) that the electron enters the slit, measured from the normal to the slit plane; $r = r_0(1 + \xi)$ where r_0 is the mean radius; and

$$(\Delta E/E_0) = (E - E_0/E_0),$$

where E_0 is the analyzer pass energy. It is clear that the image position, ξ_{EXIT}, is a nonlinear function of E over the detector plane, and that ξ_{EXIT} is also affected by the angular spread $\Delta\alpha$ of the beam that is admitted into the entrance slit. The departure of measured peak position from the theoretically predicted position is very small (a few percent); this property of hemispherical analyzers has also been discussed in some detail by Gurney *et al.*[26] The measured energy dis-

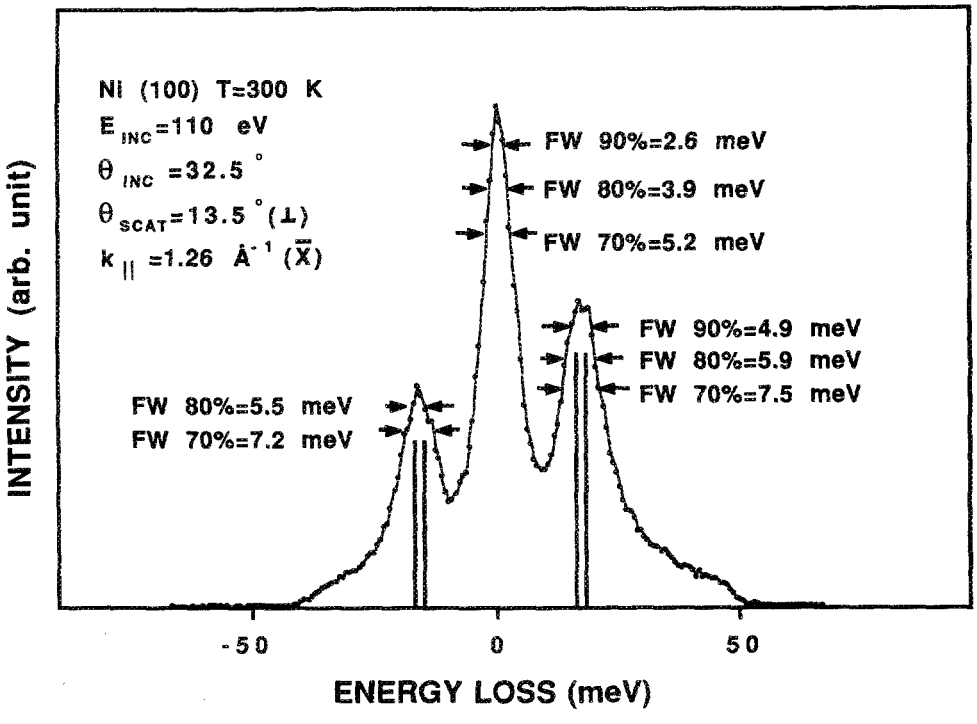

FIG. 10. EELS spectra for Ni(100) at X of the two-dimensional Brillouin zone measured in out-of-plane scattering geometry. In this case, incident $k_{\parallel}$ is equal to a reciprocal lattice vector G_1, the scattered $k_{\parallel}$ is at X. The loss and gain peaks consist of two losses resulting from the S_1 and S_4 surface phonons. The additional width of loss and gain features relative to the elastic peak is attributed to two closely spaced losses resulting from the S_4 and S_1 surface phonons.

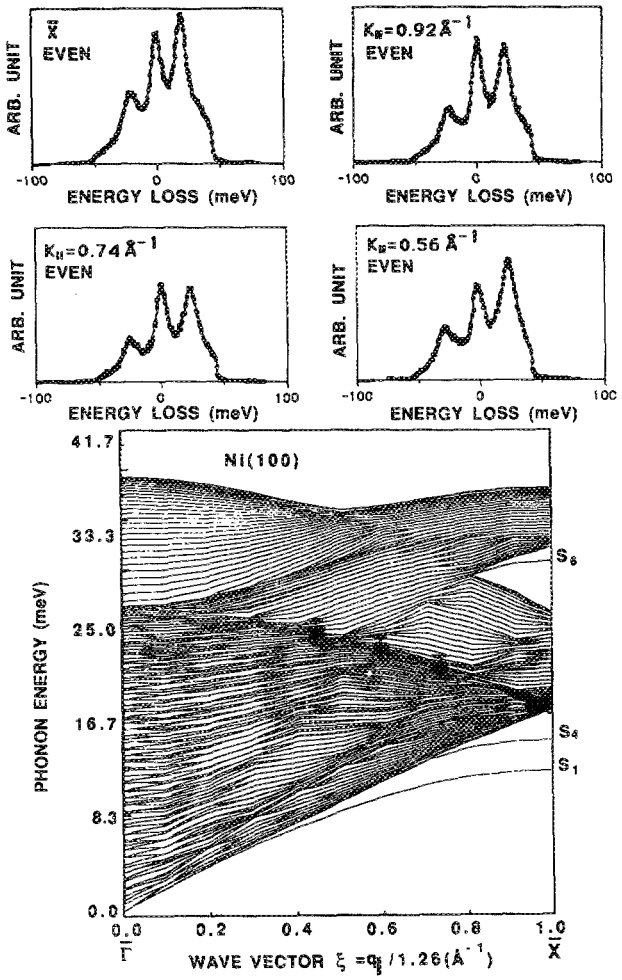

FIG. 11. Upper panel: EELS spectra taken in even symmetry geometry at four value of $k_{\parallel}$. $E_{inc} = 150$ eV. In all cases, $\theta_i \cong 0$ and θ_s was adjusted to yield desired $k_{\parallel}$. Lower panel: calculated phonons of a 61 layer slab (Tong *et al.*, Ref. 53). The location of loss peaks in the bulk continuum are shown on the dispersion curves (refer to text).

persion across the detector plane is actually closer to linear behavior than theoretically predicted.

Figure 10 displays an EELS spectrum for Ni(100) at $\bar{X}$ taken at T = 300 K and energy resolution ~6 meV ($E_i = 1.2$ eV). (In direct beam geometry, the same operating conditions yield energy resolution of ~4 meV.) This data was taken in out-of-plane scattering geometry which permits observation of both even (S_4) and odd (S_1) symmetry modes. The analyzer slit voltage was fixed; therefore, the spectrum reflects minor variations in channel plate gain over the face as well as the small variation in energies near the detector edges. Loss and gain peaks at $\pm$ 16.6 meV and shoulders at $\pm$ 14.3 meV correspond to the S_4 phonon and S_1 phonon, respectively. The S_4 phonon energy at $\bar{X}$ is in good agreement with previous work,[4] and the S_1 phonon energy which has not been previously detected experimentally is in good agreement with recent calculations.[53] The spectrum consists of "raw" data—no smoothing or other processing has been applied. Typical counting rates for surface phonon spectra are ~1 kHz. Direct comparison of this counting rate with other instruments requires taking into account not only the energy resolution ~6 meV, but also the angular resolution of the incident and collected beam. The real apertures and lens voltages used in tests and EELS spectra reported in this article yield a true angular resolution of 0.1° corresponding to $\Delta k_{\parallel} \sim \pm 0.01$ Å at $E_{inc} = 155$ eV. The instrument response function (convoluted monochromator and analyzer response corresponding to the elastic peak) is fit better using a Lorentzian rather than a Gaussian function. With the high sensitivity available from the multichannel detection, excellent statistics can be obtained in a few minutes. Even though the full width at half maximum resolution indicated in Fig. 10 is only 6 meV, the excellent statistics and sharply peaked instrument response function nearly resolve the S_1 and S_4 modes which are separated in energy by only 2 meV. Simple curve fitting procedures illustrated in Fig. 10 show that at least two modes are required to account for the loss and gain peak widths. A narrower single (S_4) mode is detected in even scattering geometry.

Note that when the energy resolution is increased by lowering the pass energy of *both* the monochromator and analyzer, the decrease in counting rate of the multichannel detection spectrometer is typically less than a single channel instrument. As long as the analyzer energy window (256 meV at 1.2-eV pass energy) is less than the total width of the loss plus gain features (typically 60 meV), the only loss in intensity results from the decrease in monochromator current that accompanies a lower pass energy.

Figure 11(a) displays four EELS spectra for Ni(100) at $k_{\parallel}$ along $\bar{\Gamma} - \bar{X}$. These spectra were taken in even symmetry scattering geometry. The angles describing incident and scattered directions were chosen to be near normal. In this geometry, for a given electron mean free path at $E_{inc} = 125$ eV, scattered electrons will probe deeper in the crystal than for more grazing angles. Figure 11(b) reproduces the calculated phonon spectrum for a 61 layer slab Ni(100) along $\bar{\Gamma}$-$\bar{X}$ reported by Tong *et al.*[53] The vibrational bands represent all of the film normal modes, both surface modes and modes within the slab. The slab is thick enough that bulk modes of an infinite crystal are modeled fairly accurately. The S_1 (shear horizontal mode) is normally not seen in in-plane (even) symmetry scattering geometry because of selection rules. This mode is apparent in the spectra of Fig. 10 along with the S_4 (Rayleigh mode) which is a vertical displacement mode. Both the S_1 and S_4 modes are true surface modes having eigen vectors confined primarily to top layer atoms. A third surface mode (S_6) exists in the gap at $\bar{X}$. This mode is also a shear displacement mode, having even symmetry and can be detected in even scattering geometry at suitable incident energies.

A particularly interesting feature of the data shown in Fig. 11(a) is that the loss peaks (and corresponding gain peaks) occur at energies and values of $k_{\parallel}$ that lie in the slab continuum (i.e., the projected bulk bands). The location of these four peaks is indicated on Fig. 11(b). Clearly, under the particular kinematic conditions selected for these spectra (high energy, $\theta_i + \theta_s < 40°$) the surface modes ($S_4$ in particular which is normally always detected) are not seen. The cross section of surface modes is effectively suppressed and what is observed are the inelastic losses corresponding to bulk modes having a high density of states at the value of $k_{\parallel}$

determined by the scattering geometry. This behavior is clear evidence that scattering conditions can be chosen to emphasize bulk phonon modes. Clearly, phonon modes at shallow interfaces will be accessible using inelastic electron scattering. This is one application that helium scattering will not be able to address.

ACKNOWLEDGMENTS

The authors wish to thank Les Deavers and Danny Boyd of the Physics Department Machine Shop for constructing the electron optics, and Joe Comunale, Abdelkrim Sellidj, Joan Yater, and Fawzi Hadjarab for preparing engineering drawings and other valuable assistance. This work was sponsored by AFOSR-86-0109 and The Robert A. Welch Foundation.

[1]H. Froitzheim, in *Topics in Current Physics*, edited by H. Ibach (Springer, New York, 1976), Vol. 4.
[2]H. Ibach and D. L. Mills, in *Electron Energy Loss Spectroscopy and Surface Vibrations* (Academic, New York, 1982).
[3]J. L. Erskine, CRC Critical Reviews **13**, 311 (1987).
[4]M. Rocca, H. Ibach, S. Lehwald, and T. S. Rahman, in *Topics in Current Physics*, edited by W. Schommers and P. Von Blackenhagen (Springer, Berlin, 1986), Vol. 41.
[5]R. Caudano, J. M. Gilles, and A. A. Lucas, Eds., *Vibrations at Surfaces* (Plenum, New York, 1982).
[6]C. R. Brundle and H. Morawitz, Eds., *Vibrations at Surfaces* (Elsevier, Amsterdam, 1983).
[7]D. A. King, N. V. Richardson, and S. Holloway, Eds., *Vibrations at Surfaces* (Elsevier, Amsterdam, 1986).
[8]M. L. Xu, B. M. Hall, S. Y. Tong, M. Rocca, H. Ibach, S. Lehwald, and J. E. Black, Phys. Rev. Lett. **54**, 1171 (1985).
[9]R. E. Allen, G. P. Aldredge, and F. W. deWette, Phys. Rev. B **4**, 1648 (1971); **4**, 1661 (1971); **4**, 1682 (197); F. W. deWette and G. P. Aldredge, *Methods in Computational Physics* (Academic, New York, 1976), Vol. 15.
[10]R. L. Strong and J. L. Erskine, Phys. Rev. B **31**, 6305 (1985); Phys. Rev. Lett. **54**, 346 (1985); T. S. Rahman, J. E. Black, and D. L. Mills, Phys. Rev. B **25**, 883 (1982).
[11]L. L. Kesmodel, M. L. Xu, and S. Y. Tong, Phys. Rev. B **34**, 2010 (1986).
[12]C. Oshima, R. Souda, M. Aono, S. Otani, and Y. Ishizawa, Phys. Rev. B **30**, 5361 (1984).
[13]H. Ibach, in *Proceedings of the Solvay Conference on Surface Science*, edited by F. W. deWette (Springer, Berlin, 1988).
[14]U. Harten, J. P. Toennies, and Ch. Woll, Faraday Discuss. Chem. Soc. **80**, 137 (1985).
[15]K. D. Gibson and S. J. Sibener, Faraday Discuss. Chem. Soc. **80**, 203 (1985).
[16]S. Nagano, Z.-P. Luo, H. Metin, W. M. Huo, and V. McKoy, J. Chem. Phys. **88**, 7970 (1988); **85**, 7970 (1986); Surf. Sci. Lett. **186**, L548 (1987).
[17]S. Y. Tong, C. H. Li, and D. L. Mills, Phys. Rev. B **24**, 806 (1981).
[18]H. Conrad, R. Scala, W. Stenzel, and R. Unwin, J. Chem. Phys. **81**, 6371 (1984); H. Conrad, M. E. Kordesch, R. Scala, and W. Stenzel, J. Electron Spectrosc. Relat. Phenom. **38**, 289 (1986).
[19]L. J. Richter, T. A. Germer, J. P. Sethna, and W. Ho, Phys. Rev. B (in press).
[20]A. A. Lucas and M. Sunjic, Phys. Rev. Lett. **26**, 229 (1971); Prog. Surf. Sci. **2**, 2 (1972); E. Evans and D. L. Mills, Phys. Rev. B **5**, 4126 (1972); B. J. N. Persson, Solid State Commun. **24**, 573 (1977); D. Sokcevic, Z. Lenac, R. Brako, and M. Sunjic, J. Phys. **28**, 273 (1977); F. Delanaye, A. Lucas, and G. D. Mahan, Surf. Sci. **70**, 629 (1978); W. L. Schaich, Phys. Rev. B **24**, 686 (1981); Surf. Sci. **122**, 175 (1982).
[21]V. Roundy and D. L. Mills, Phys. Rev. B **5**, 1347 (1972).
[22]F. M. Propst and T. C. Piper, J. Vac. Sci. Technol. **4**, 53 (1966).
[23]H. Froitzheim, H. Ibach, and S. Lehwald, Rev. Sci. Instrum. **46**, 132 (1975).
[24]S. Lehwald, J. M. Szeftel, H. Ibach, T. S. Rahman, and D. L. Mills, Phys. Rev. Lett. **50**, 518 (1983).
[25]W. Ho, J. Vac. Sci. Technol. A **3**, 1432 (1985); J. Phys. Chem. **91**, 766(1987); J. Electron Spectrosc. Relat. Phenom. **45**, 1 (1987); L. J. Richter, W. D. Micher, L. J. Whitman, W. A. Noonan, and W. Ho, Rev. Sci. Instrum. **60**, 12 (1989).
[26]B. A. Gurney, W. Ho, L. J. Richter, and J. S. Villarrubia, Rev. Sci. Instrum. **59**, 22 (1988).
[27]R. Franchy and H. Ibach, Surf. Sci. **155**, 15 (1985).
[28]G. W. Fraser, Nucl. Instrum. Methods, Phys. Res. **221**, 115 (1984).
[29]L. J. Richter and W. Ho, Rev. Sci. Instrum. **57**, 1469 (1986).
[30]L. Asplund, U. Geliens, P. A. Tove, S. A. Eriksson, and N. Bingefors, Nucl. Instrum. Methods Phys. Res. **226**, 204 (1984).
[31]S. D. Kevan and L. H. Dubois, Rev. Sci. Instrum. **55**, 1604 (1984).
[32]S. Lehwald and H. Ibach, in *Vibrations at Surfaces*, edited by R. Caudano, J. M. Gilles, and A. A. Lucas (Plenum, New York, 1982).
[33]L. L. Kesmodel, J. Vac. Sci. Technol. A **1**, 1456 (1983).
[34]H. Froitzheim, J. Electron Spectrosc. Relat. Phenom. **34**, 11 (1984).
[35]R. Unwin, W. Stenzel, A. Garbout, and H. Conrad, Rev. Sci. Instrum. **55**, 1809 (1984).
[36]C. E. Kuyatt and J. R. Simpson, Rev. Sci. Instrum. **38**, 103 (1967); J. Appl. Phys. **37**, 3805 (1966).
[37]H. Froitzheim, Diplomarbeit, Technischen Hochschnle Aachen (1971).
[38]H. Wollnik and H. Ewald, Nucl. Instrum. Methods **36**, 93 (1965).
[39]R. Herzog, Z. Phys. **97**, 596 (1935); **41**, 18 (1940).
[40]H. D. Polaschegg, Appl. Phys. **9**, 223 (1976).
[41]Surface Science Labs (Model 3390 OPT SA), 465 National Avenue, Mountain View, CA 94043, (415) 962-8767.
[42]F. Hadjarab and J. L. Erskine, J. Electron Spectrosc. Relat. Phenom. **36**, 227 (1985).
[43]S. Nishigaki and S. Kanasi, Rev. Sci. Instrum. **57**, 225 (1986).
[44]K. Jost, J. Phys. E **12**, 1001 (1979); J. E. Pollard, D. J. Trevor, Y. T. Lee, and D. A. Shirley, Rev. Sci. Instrum. **52**, 1837 (1981).
[45]E. -J. Jeong and J. L. Erskine (unpublished).
[46]C. Oshima, R. Souda, M. Aono, and Y. Ishizawa, Rev. Sci. Instrum. **56**, 227 (1985).
[47]S. D. Kevan, Rev. Sci. Instrum. **54**, 1441 (1983).
[48]A. Sellidj, M. A. Thesis, University of Texas, 1986 (to be published).
[49]G. Martinez and M. Sancho, J. Phys. E. **16**, 625 (1983).
[50]G. Martinez, M. Sancho, and F. H. Reed, J. Phys. E. **16**, 632 (1983).
[51]D. W. O. Heddle and N. Papadovassilakis, J. Phys. E. **17**, 599 (1984).
[52]A. Sellidj and J. L. Erskine (unpublished).
[53]S. Y. Tong, Y. Chen, J. M. Yao, and Z. Q. Wu, Phys. Rev. (to be published).